Optical Engineering

SPIEDigitalLibrary.org/oe

Polarization spatial heterodyne interferometer: model and calibration

Michael W. Kudenov
Matthew N. Miskiewicz
Michael J. Escuti
James F. Coward

SPIE

Polarization spatial heterodyne interferometer: model and calibration

Michael W. Kudenov,[a,*] Matthew N. Miskiewicz,[a] Michael J. Escuti,[a] and James F. Coward[b]
[a]North Carolina State University, Department of Electrical and Computer Engineering, 2410 Campus Shore Drive, Raleigh, North Carolina 27606
[b]SA Photonics, 130 Knowles Drive Suite A, Los Gatos, California 95032

Abstract. Spatial heterodyne interferometry (SHI) is a technique based on Fourier transform spectroscopy. As such, many of the benefits, such as high spectral resolving power, can be realized. Furthermore, unlike a Fourier transform spectrometer, an SHI is able to minimize the number of required samples for a given resolving power and spectral range. The calibration and detailed modeling of a polarization spatial heterodyne interferometer (PSHI) are detailed. Unlike our original first-order ray tracing model, the new model is based on the Jones matrix formalism. Using this improved model, we explore the nonideal aspects of the PSHI, including interference effects caused by retardance errors in the polarization grating and quarter wave plate. To minimize the influence of these errors, a calibration procedure is described based on a linear operator theory. Finally, the Jones matrix model and calibration procedure are validated through a series of simulations and experiments. [DOI: 10.1117/1.OE.53.4.044104]

Keywords: interferometry; polarization; birefringence; heterodyning; spectrometers.

Paper 140166P received Jan. 29, 2014; revised manuscript received Mar. 10, 2014; accepted for publication Mar. 13, 2014; published online Apr. 8, 2014.

1 Introduction

Fourier transform spectrometers (FTSs) are well known for their high spectral resolving power.[1,2] Typically, high spectral resolution measurements are based on Michelson interferometers. Although these offer measurement flexibility, high throughput, and spectral resolution, disadvantages include vibration sensitivity, temporal and mechanical scanning requirements, and alignment sensitivity. Fortunately, vibration sensitivity and the need for mechanical scanning can be overcome with common-path interferometers.[3] These sensors map optical path difference (OPD) across a two-dimensional (2-D) focal plane array (FPA) or line array (LA) camera such that

$$\mathrm{OPD}(x,y) \propto ay + b, \tag{1}$$

where a is the slope and b is the offset. This enables multiple interferogram samples to be acquired simultaneously, enhancing the speed of the spectral measurement.

One issue with conventional FTS implementations, including common-path systems, is sampling inefficiency. For instance, a conventional nonaliased FTS must resolve all wave numbers to fully measure a spectrum.[4] This limitation is best observed with an example. Consider a conventional FTS, designed to measure the atmospheric oxygen emission within the spectral band of 558 ± 3 nm (e.g., 17,825 to 18,018 cm^{-1}) to infer atmospheric wind speed and temperature.[5–8] Assuming that a complete interferogram is required (i.e., not the partial interferograms described in Refs. 5–8), then the required spectral resolution $\Delta\sigma$ of the system is approximately 1.0 cm^{-1}. If the spectrometer's cutoff frequency were 540 nm (18,519 cm^{-1}), then the FTS must measure all spectral points spanning 0 cm^{-1} to the Nyquist frequency. Therefore, while only 193 samples within the region of the emission line are actually of interest, approximately 18,519 samples, assuming a single-sided interferogram, are required to acquire the region of interest. Ultimately, this value would be slightly greater, since a small double-sided region is required for phase correction.[1]

Although sampling inefficiencies can be overcome in a conventional Michelson interferometer by aliasing the interferogram's measurement,[9] this is not a viable option with most FPA- or LA-based FTSs. Given a pixel width of d_w, the interference's spatial frequency η_I in units of cycles/pixel, generated by the OPD defined in Eq. (1), can be expressed as

$$\eta_I = a\sigma d_w, \tag{2}$$

where σ is the wave number. Since each pixel has a finite optical transfer function, the interference fringe's visibility will generally decrease with increasing spatial frequency. Interference visibility is defined as

$$V = (I_{\max} - I_{\min})/(I_{\max} + I_{\min}), \tag{3}$$

where $I_{\max}$ and $I_{\min}$ are the maximum and minimum intensities within a local fringe. This tradeoff is illustrated in Fig. 1, which depicts V versus spatial frequency η_I. Note that this analysis assumes a pixel pitch that is equal to the pixel width.

Revisiting the previous oxygen emission example demonstrates the impracticality of the aliasing technique when using detector arrays. Assuming a linear array is used with a pixel pitch of d_w means that the required slope of the OPD can be expressed as

*Address all correspondence to: Michael Kudenov, E-mail: mwkudeno@ncsu.edu

0091-3286/2014/$25.00

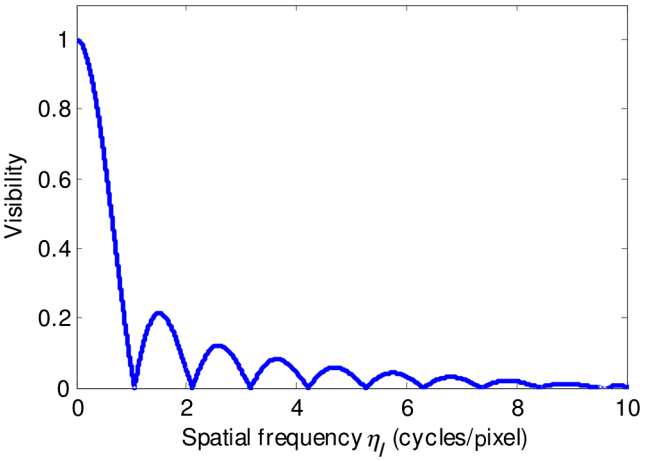

Fig. 1 Fringe visibility versus the interferogram's spatial frequency.

$$a = 1/(\Delta\sigma N_s d_w), \tag{4}$$

where N_s is the number of samples in the interferogram. Substituting Eq. (4) into Eq. (2) yields a normalized spatial frequency of

$$\eta_I = \sigma/(\Delta\sigma N_s). \tag{5}$$

Given $N_s = 18{,}519$ yields $\eta_I = 1.0$ cycles/pixel, resulting in zero fringe visibility per Fig. 1. Ideally the spatial frequency must be decreased in order to increase the detector's response. However, the issue is only worsened when using the aliasing technique. For instance, if aliasing is implemented on a 1000 pixels array, then $\eta_I = 17.9$ cycles/pixel. Thus, while the spatial frequency is aliased, its visibility is too low to remain detectable.

Two techniques exist to increase the spectral resolution in these common-path instruments while minimizing the number of samples required: (1) modifying the offset b while maintaining a resolvable slope a or (2) heterodyning the interference to lower spatial frequencies.[4,10,11] Since modifying b does little to negate the sampling limitation, we consider spatial heterodyning in the current approach. A spatial heterodyne interferometer (SHI) is able to conserve the high spectral resolution of conventional FTS systems.[5–8] They do so by replacing the retro-reflecting mirrors of a Michelson interferometer with Littrow-configured blazed diffraction gratings.[5,11] This enables any arbitrary wave number, σ_h, to generate a 0 cycle/m interference fringe, where σ_h is the heterodyne wave number (note that in the conventional nonaliased FTS, $\sigma_h = 0$ cm^{-1}).

The implementation of SHI has primarily leveraged the Michelson interferometer (MI) architecture.[7,8] In these systems, the MIs vibration and thermal errors have been addressed by creating monolithic all-glass systems. Alternatives to this technique, which aim to create common-path vibration insensitive designs, are based on Sagnac interferometers.[12,13] However, to minimize both size and vibration sensitivity, SHIs based on fiber-optic Mach–Zehnder interferometers[14] and an SHI system based on birefringent prisms and polarization gratings (PGs)[15,16] have also been introduced. With these implementations, the interferometer's size, weight, and alignment complexity can be significantly reduced over reflective free-space Sagnac interferometers or uncommon-path monolithic Michelson interferometer designs.

In this paper, we focus on advancing the modeling and calibration procedures of a polarization spatial heterodyne interferometer (PSHI) that was originally presented in Ref. 15. Advantages of this architecture lie in its potential compactness, due to the use of monolithic birefringent crystals, and its vibration insensitivity, stemming from its common-path design.[17,18] In Sec. 2, we discuss a Jones matrix model of the PSHI and investigate its nonideal properties. In Sec. 3, we present our experimental system while Sec. 4 contains the experimental measurements that are used to validate the model. Finally, in Sec. 5, we discuss the methods of calibration and experimentally demonstrate the calibration procedure, validating it against a separate spectral measurement.

2 Theoretical Model

The goal of our theoretical model is to understand the nonideal characteristics that arise when performing spatial heterodyning with a PG.[16] In the PSHI, interference cross talk was caused by the PG's unwanted diffraction orders.[15] These orders are presented in Fig. 2, superimposed on the schematic of the original PSHI system. Polarized light initially transmits through a Wollaston prism (WP), with an apex angle α, which causes the two incident polarization states to split at an angle θ_{WP}. These beams are then incident on a quarter wave plate (QWP). The QWP has a fast axis orientation of 45 deg with respect to the x, such that the orthogonal linear eigenpolarizations of the WP are converted into orthogonal circular polarization states. These states interact with the PG and are subsequently diffracted into either the $m = 0$ or $m = \pm 1$ diffraction orders. A linear analyzer (A) unifies the polarization state, enabling interference to be measured on the FPA.

Ideally, after the WP's light transmits through the PG, only the two $m = -1$ order beams, with angular separation θ_d (e.g., an angularly reduced component compared to θ_{WP}), should exist. However, the PG's zero-order light leakage allows two unwanted beams to propagate with an angular separation of θ_0, such that $\theta_0 = \theta_{\mathrm{WP}}$. Furthermore, error in the QWP's retardance will cause some light to be coupled into the $m = +1$ order, creating two additional unwanted beams propagating at an angle θ_u with respect to each other. Finally, the cross terms, denoted as θ_{c1}, θ_{c2}, and θ_{c3}, also create observable interference effects. Under the small angle approximation, the angle of diffraction from the PG can be expressed as

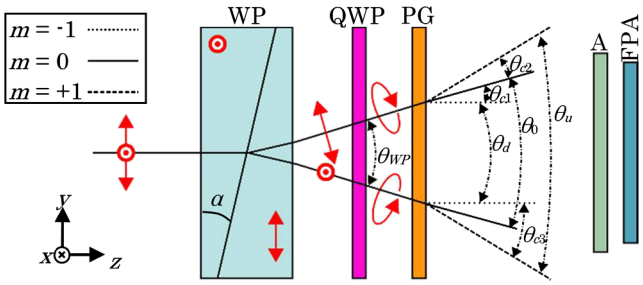

Fig. 2 Schematic of the beams exiting the PSHI.

$$\theta_m = \theta_{\mathrm{WP}} + \frac{m\lambda}{\Lambda}, \tag{6}$$

where Λ is the PG's spatial period and λ is the free-space wavelength. Due to the linearity of Eq. (6), $\theta_{c1} = \theta_{c2}$ and $\theta_{c3} = 2\theta_{c1}$.

The Jones matrix formalism[19] was used to model the interference created by the beams exiting the PG. For a WP, the Jones matrix can be expressed as

$$\mathbf{J}_{\mathrm{WP}} = \begin{pmatrix} 1 & 0 \\ 0 & e^{iU_{\mathrm{WP}}} \end{pmatrix}, \tag{7}$$

where U_{WP} is the spatially dependent phase delay imparted to the polarization states by the WP. This term can be expressed as

$$U_{\mathrm{WP}} = 4\,\pi\sigma\Delta n_C\,\tan(\alpha)y, \tag{8}$$

where α is the prism's apex angle, $\sigma = 1/\lambda$ is the wave number, and Δn_C is the birefringence of the prism's crystal such that

$$\Delta n_C = (n_{e,C} - n_{o,C}), \tag{9}$$

where $n_{e,C}$ and $n_{o,C}$ are the crystal's extraordinary and ordinary refractive indices, respectively. Meanwhile, the Jones matrix for a general retarder is

$$\mathbf{J}_{\mathrm{Ret}}(\theta,\phi) = \begin{pmatrix} A & B \\ B & C \end{pmatrix}, \tag{10}$$

in which

$$A = \cos^2(\theta) + \exp[i\phi]\sin^2(\theta), \tag{11}$$

$$B = \cos(\theta)\sin(\theta) - \exp[i\phi]\cos(\theta)\sin(\theta), \tag{12}$$

and

$$C = \exp[i\phi]\cos^2(\theta)\sin^2(\theta), \tag{13}$$

where θ is the fast axis orientation angle in the xy-plane and ϕ is the retardance. The Jones matrix for the PG can be expressed using $\phi = \phi_{\mathrm{PG}}$ with a fast axis angle $\theta = U_{\mathrm{PG}}$ such that

$$U_{\mathrm{PG}} = 2\,\pi y/\Lambda, \tag{14}$$

where U_{PG} is the PG's spatially dependent phase term, ϕ_{PG} is the retardance of the liquid crystal layer, and Λ is the PG's spatial period.[20,21] The spatial frequencies of the WP and PG can be expressed as

$$\eta_{\mathrm{WP}} = 2\sigma\Delta n_C\tan(\alpha), \tag{15}$$

and

$$\eta_{\mathrm{PG}} = 1/\Lambda, \tag{16}$$

respectively. Meanwhile, the retardance of the PG's polymerized liquid crystal layer can be expressed as

$$\phi_{\mathrm{PG}} = 2\pi\sigma d_{\mathrm{LC}}\Delta n_{\mathrm{LC}}, \tag{17}$$

where d_{LC} is the liquid crystal layer's thickness and Δn_{LC} is the liquid crystal's birefringence such that

$$\Delta n_{\mathrm{LC}} = (n_{e,\mathrm{LC}} - n_{o,\mathrm{LC}}), \tag{18}$$

where $n_{e,\mathrm{LC}}$ and $n_{o,\mathrm{LC}}$ are the extraordinary and ordinary refractive indices of the liquid crystal. The refractive indices of the RMS03-001C (Merck) reactive mesogen, according to the vendor's datasheet, are

$$n_{e,\mathrm{LC}} = 1.629 + 18350/\lambda^2, \tag{19}$$

and

$$n_{o,\mathrm{LC}} = 1.501 + 10010/\lambda^2, \tag{20}$$

where the wavelength λ is in nm. It should be mentioned that the dispersion in ϕ_{PG} is the primary contributor to error addressed in the current paper.

Meanwhile, the QWP can be expressed using Eq. (10) with $\phi = \phi_{\mathrm{QWP}}$ and $\theta = \theta_{\mathrm{QWP}}$, where θ_{QWP} and ϕ_{QWP} are the QWPs orientation and retardance, respectively. The Jones matrix for a linear polarizer, with a transmission axis oriented at 0 deg with respect to the x-axis, is

$$\mathbf{J}_{\mathbf{LP}} = \begin{pmatrix} 1 & 0 \\ 0 & 0 \end{pmatrix}. \tag{21}$$

Calculating the electric field incident onto the detector can be accomplished by

$$\mathbf{E}_{\mathrm{out}} = \mathbf{J}_{\mathrm{LP}} \cdot \mathbf{J}_{\mathrm{PG}} \cdot \mathbf{J}_{\mathrm{QWP}} \cdot \mathbf{J}_{\mathrm{WP}} \cdot \mathbf{E}_{\mathrm{in}}. \tag{22}$$

Using a 45-deg linearly polarized input makes

$$\mathbf{E}_{\mathrm{in}} = E(\sigma)[\,1/\sqrt{2} \quad 1/\sqrt{2}\,]^{\mathrm{T}}, \tag{23}$$

where the superscript T represents the transpose operation and $E(\sigma)$ represents the incident spectrum's complex amplitude at a specific wave number. Setting $\theta_{\mathrm{QWP}} = \pm 45$ deg while maintaining generality with ϕ_{PG} and ϕ_{QWP} enables the intensity, detected by the FPA, to be calculated as

$$I_{\mathrm{out}}(x,y,\sigma) = \left|\mathbf{E}_{\mathrm{out}}\right|^2 = 16\left|E(\sigma)\right|^2 + I_0(x,y,\sigma) + I_{c1}(x,y,\sigma) + I_d(x,y,\sigma) + I_{c3}(x,y,\sigma) + I_u(x,y,\sigma), \tag{24}$$

where I_0, I_{c1}, I_d, I_{c3}, and I_u represent the interference between the beams corresponding to the angles θ_0, θ_{c1}, θ_d, θ_{c3}, and θ_u, respectively, per Fig. 2. The intensity of these components can be represented as

$$\begin{aligned} I_0(x,y,\sigma) = 2\left|E(\sigma)\right|^2 [&\pm\cos(U_{\mathrm{WP}} - \phi_{\mathrm{PG}} - \phi_{\mathrm{QWP}}) \\ &\mp\cos(U_{\mathrm{WP}} - \phi_{\mathrm{PG}} + \phi_{\mathrm{QWP}}) \pm\cos(U_{\mathrm{WP}} + \phi_{\mathrm{PG}} - \phi_{\mathrm{QWP}}) \\ &\mp\cos(U_{\mathrm{WP}} + \phi_{\mathrm{PG}} + \phi_{\mathrm{QWP}}) \pm 2\,\cos(U_{\mathrm{WP}} + \phi_{\mathrm{QWP}}) \\ &\pm 2\,\cos(U_{\mathrm{WP}} - \phi_{\mathrm{QWP}})], \end{aligned} \tag{25}$$

$$I_{c1}(x,y) = 2\left|E(\sigma)\right|^2[\sin(U_{\mathrm{WP}} - U_{\mathrm{PG}} + \phi_{\mathrm{PG}} + \phi_{\mathrm{QWP}}) - \sin(U_{\mathrm{WP}} - U_{\mathrm{PG}} - \phi_{\mathrm{PG}} - \phi_{\mathrm{QWP}}) + \sin(U_{\mathrm{WP}} - U_{\mathrm{PG}} + \phi_{\mathrm{PG}} - \phi_{\mathrm{QWP}}) - \sin(U_{\mathrm{WP}} - U_{\mathrm{PG}} - \phi_{\mathrm{PG}} + \phi_{\mathrm{QWP}})], \tag{26}$$

$$I_d(x,y) = |E(\sigma)|^2[\pm\cos(U_{\mathrm{WP}} - 2U_{\mathrm{PG}} + \phi_{\mathrm{PG}} + \phi_{\mathrm{QWP}}) \mp\cos(U_{\mathrm{WP}} - 2U_{\mathrm{PG}} + \phi_{\mathrm{PG}} - \phi_{\mathrm{QWP}}) \mp\cos(U_{\mathrm{WP}} - 2U_{\mathrm{PG}} - \phi_{\mathrm{PG}} + \phi_{\mathrm{QWP}}) \mp\cos(U_{\mathrm{WP}} - 2U_{\mathrm{PG}} - \phi_{\mathrm{PG}} - \phi_{\mathrm{QWP}}) \mp 2\cos(U_{\mathrm{WP}} - 2U_{\mathrm{PG}} + \phi_{\mathrm{QWP}}) \pm 2\cos(U_{\mathrm{WP}} - 2U_{\mathrm{PG}} - \phi_{\mathrm{QWP}}) - 4\sin(U_{\mathrm{WP}} - 2U_{\mathrm{PG}}) + 2\sin(U_{\mathrm{WP}} - 2U_{\mathrm{PG}} - \phi_{\mathrm{PG}}) + 2\sin(U_{\mathrm{WP}} - 2U_{\mathrm{PG}} + \phi_{\mathrm{PG}})], \tag{27}$$

$$I_{c3}(x,y) = 2|E(\sigma)|^2[\sin(U_{\mathrm{WP}} + U_{\mathrm{PG}} + \phi_{\mathrm{PG}} + \phi_{\mathrm{QWP}}) - \sin(U_{\mathrm{WP}} + U_{\mathrm{PG}} - \phi_{\mathrm{PG}} - \phi_{\mathrm{QWP}}) + \sin(U_{\mathrm{WP}} + U_{\mathrm{PG}} - \phi_{\mathrm{PG}} - \phi_{\mathrm{QWP}}) - \sin(U_{\mathrm{WP}} + U_{\mathrm{PG}} - \phi_{\mathrm{PG}} + \phi_{\mathrm{QWP}})], \tag{28}$$

and

$$I_u(x,y) = \left|E(\sigma)\right|^2[\pm\cos(U_{\mathrm{WP}} + 2U_{\mathrm{PG}} + \phi_{\mathrm{PG}} + \phi_{\mathrm{QWP}}) \mp\cos(U_{\mathrm{WP}} + 2U_{\mathrm{PG}} + \phi_{\mathrm{PG}} - \phi_{\mathrm{QWP}}) \pm\cos(U_{\mathrm{WP}} + 2U_{\mathrm{PG}} - \phi_{\mathrm{PG}} + \phi_{\mathrm{QWP}}) \mp\cos(U_{\mathrm{WP}} + 2U_{\mathrm{PG}} - \phi_{\mathrm{PG}} + \phi_{\mathrm{QWP}}) \mp 2\cos(U_{\mathrm{WP}} + 2U_{\mathrm{PG}} + \phi_{\mathrm{QWP}}) \pm 2\cos(U_{\mathrm{WP}} + 2U_{\mathrm{PG}} - \phi_{\mathrm{QWP}}) + 4\sin(U_{\mathrm{WP}} + 2U_{\mathrm{PG}}) - 2\sin(U_{\mathrm{WP}} + 2U_{\mathrm{PG}} + \phi_{\mathrm{PG}}) - 2\sin(U_{\mathrm{WP}} + 2U_{\mathrm{PG}} - \phi_{\mathrm{PG}})]. \tag{29}$$

It should be mentioned that Eqs. (25)–(29) assume negligible ±2nd-order diffraction, which was measured at 0.21% in our experimental PG. Expanding the discussion to continuous spectral distributions means that Eq. (24) can be spectrally band-integrated such that

$$I(x,y) = \int T(x,y,\sigma)R(x,y,\sigma)I_{\mathrm{out}}(x,y,\sigma)\mathrm{d}\sigma, \tag{30}$$

where $T(x,y,\sigma)$ is the transmission of the optics and $R(x,y,\sigma)$ is the responsivity of the detector. Fourier transformation of Eq. (30) yields five frequency components, corresponding to the Fourier transformation of Eqs. (25)–(29). Since the calculation of these transforms is straightforward and providing their rigorous closed form representations offers limited utility, we have expressed only their proportionalities for clarity. The Fourier transformations of Eqs. (25)–(29) are

$$F_0(x,y) \propto \int |E(\sigma)|^2 * \left[A_0(\sigma)\delta\delta\left(\frac{\sigma}{\eta_{\mathrm{WP}}}\right)\right]\mathrm{d}\sigma, \tag{31}$$

$$F_{c1}(x,y) \propto \int |E(\sigma)|^2 * \left[A_{c1}(\sigma)\delta\delta\left(\frac{\sigma}{\eta_{\mathrm{WP}} - \eta_{\mathrm{PG}}}\right)\right]\mathrm{d}\sigma, \tag{32}$$

$$F_d(x,y) \propto \int |E(\sigma)|^2 * \left[A_d(\sigma)\delta\delta\left(\frac{\sigma}{\eta_{\mathrm{WP}} - 2\eta_{\mathrm{PG}}}\right)\right]\mathrm{d}\sigma, \tag{33}$$

$$F_{c3}(x,y) \propto \int |E(\sigma)|^2 * \left[A_{c3}(\sigma)\delta\delta\left(\frac{\sigma}{\eta_{\mathrm{WP}} + \eta_{\mathrm{PG}}}\right)\right]\mathrm{d}\sigma, \tag{34}$$

and

$$F_u(x,y) \propto \int |E(\sigma)|^2 * \left[A_{\mathrm{u}}(\sigma)\delta\delta\left(\frac{\sigma}{\eta_{\mathrm{WP}} + 2\eta_{\mathrm{PG}}}\right)\right]\mathrm{d}\sigma, \tag{35}$$

where A_0, A_{c1}, A_d, A_{c3}, and A_u are magnitude coefficients that are proportional to the superpositions of sinusoidal functions in Eqs. (25)–(29) and * represents a convolution. Meanwhile

$$\delta\delta(\sigma/\eta) \equiv (1/2)[\delta(\sigma + \eta) + \delta(\sigma - \eta)], \tag{36}$$

where δ is the Dirac delta function. These Fourier transform proportionalities indicate that each frequency component carries with it the power spectrum $|E(\sigma)|^2$, which is modified by the coefficients A_0, A_{c1}, A_d, A_{c3}, and A_u. In an ideal SHI, only F_d should exist and A_d would be unity for all σ. However, deviations in ϕ_{PG} and ϕ_{QWP}, away from their ideal values, yields nonzero values of A_0, A_{c1}, A_{c3}, and A_u. This creates undesired frequency components that coexist with the desired down-shifted spectrum.

2.1 *Simulated Results*

Numerical simulations were performed, using Eq. (24), to investigate the systematic effects caused by retardance errors in the PG and QWP. Double-sided interferograms were created for monochromatic spectra at wavelengths λ_0 of 460, 560, and 700 nm. A WP, with a wedge angle of $\alpha = 6.2$ deg and a PG with a period $\Lambda = 453$ μm, were used to maintain consistency with our previous experimental setup per Ref. 15. A fast Fourier transform (FFT) was applied to the simulated 1280 pixel element interferograms, along the y-dimension, such that

$$\mathrm{FF}_0(y_j,\sigma_0) = |\mathrm{FFT}(H(y)I_0(y_j,\sigma_0))|, \tag{37}$$

$$\mathrm{FF}_{c1}(y_j,\sigma_0) = |\mathrm{FFT}(H(y_j)I_{c1}(y_j,\sigma_0))|, \tag{38}$$

$$\mathrm{FF}_d(y_j,\sigma_0) = |\mathrm{FFT}(H(y_j)I_d(y_j,\sigma_0))|, \tag{39}$$

$$\mathrm{FF}_{c3}(y_j,\sigma_0) = |\mathrm{FFT}(H(y_j)I_{c3}(y_j,\sigma_0))|, \tag{40}$$

and

$$\mathrm{FF}_u(y_j,\sigma_0) = |\mathrm{FFT}(H(y_j)I_u(y_j,\sigma_0))|, \tag{41}$$

where the constant term in Eq. (24) has been removed, the x-dimension has been suppressed because interference only occurs along y, $\sigma_0 = 1/\lambda_0$, $E(\sigma_0) = 1$ for all σ_0, and the subscript j denotes y as a discrete quantity. A Hanning window, $H(y_j)$, was used to apodize the interferograms and is defined as

$$H(y_j) = 0.5(1 + \cos(\pi y_j/w)), \tag{42}$$

where $2w$ is the Hanning window's full-width.

Equations (37)–(41) were calculated for various values of ϕ_{PG} and ϕ_{QWP}. First, the WP's spatial frequency power spectrum was calculated without the PG by setting $\phi_{\mathrm{PG}} = \phi_{\mathrm{QWP}} = 0$ deg for all σ_0. This yielded the spatial frequency spectrum depicted in Fig. 3(a) in which FF_0 is the only nonzero component. For an ideal PG and QWP, $\phi_{\mathrm{PG}} = 180$ deg and $\phi_{\mathrm{QWP}} = 90$ deg for all σ_0. For these values, Figs. 3(b) and 3(c) depict the spectra that are heterodyned to both high ($\theta_{\mathrm{QWP}} = +45$ deg) and low ($\theta_{\mathrm{QWP}} = -45$ deg) spatial frequencies, respectively. Meanwhile, the spatial frequency spectrum that is obtained with error in the PG's retardance is depicted in Fig. 3(d), where $\phi_{\mathrm{PG}} = 135$ deg and $\phi_{\mathrm{QWP}} = 90$ deg. In this case, zero-order light leakage is manifested by the presence of the FF_0 component. Conversely, the result of error in the QWP's retardance is shown in Fig. 3(e), where $\phi_{\mathrm{PG}} = 180$ deg and $\phi_{\mathrm{QWP}} = 45$ deg. In this case, both the high and low spatial frequency components, corresponding to FF_u and FF_d, respectively, are present. Finally, simultaneous error in both the PG and QWP retardance values is shown in Fig. 3(f), where $\phi_{\mathrm{PG}} = 135$ deg and $\phi_{\mathrm{QWP}} = 45$ deg. Frequency components FF_0, FF_u, and FF_d are present, as well as the cross-interference terms corresponding to FF_{c1} and FF_{c3}. Notable is that the FF_{c1} component is multiplexed with the desired FF_d component.

Finally, a simulation was performed using a PG retardance spectrum that was calculated per Eq. (17) with $d_{\mathrm{LC}} = 2.05$ μm. A QWP, based on quartz crystal, was also simulated using

$$\phi_{\mathrm{QWP}} = 2\pi\sigma d_{\mathrm{QWP}}\Delta n_{\mathrm{quartz}}, \tag{43}$$

where $d_{\mathrm{QWP}} = 15.27$ μm was used for the quartz crystal's thickness. The birefringence of quartz was simulated using

$$\Delta n_{\mathrm{quartz}} = L\sigma^3 + G\sigma^2 + J\sigma + K, \tag{44}$$

where $L = 7.655\mathrm{E}-23$, $G = -3.243\mathrm{E}-16$, $J = 9.101\mathrm{E}-10$, and $K = 8.137\mathrm{E}-3$ and σ has units m^{-1}. The simulated retardance spectra for the PG and QWP are presented in Fig. 4(a) while the spatial frequency content is depicted in Fig. 4(b). Of particular importance is that the maximum

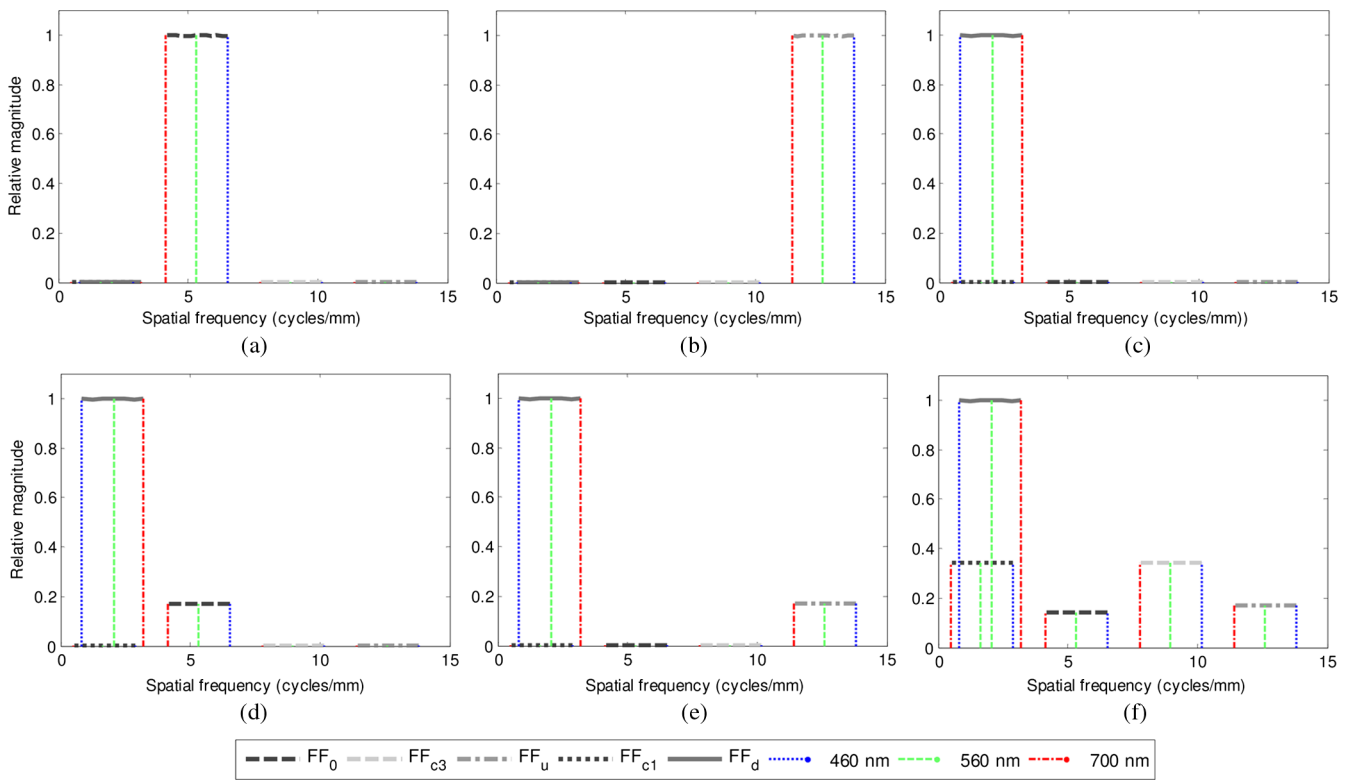

Fig. 3 Relative magnitude of the Fourier components versus spatial frequency. The three values of λ_0 are shown alongside the channel magnitudes to indicate the approximate mapping of wavelength to spatial frequency within each channel. Simulation results for (a) Wollaston prism only with $\phi_{\mathrm{PG}} = 0$ deg, $\phi_{\mathrm{QWP}} = 0$ deg. (b) Ideal up-shifted spectra with $\phi_{\mathrm{PG}} = 180$ deg, $\phi_{\mathrm{QWP}} = 90$ deg, and $\theta_{\mathrm{QWP}} = +45$ deg. (c) Ideal down-shifted spectra with $\phi_{\mathrm{PG}} = 180$ deg, $\phi_{\mathrm{QWP}} = 90$ deg, and $\theta_{\mathrm{QWP}} = -45$ deg. (d) Error in only the PGs retardance with $\phi_{\mathrm{PG}} = 135$ deg, $\phi_{\mathrm{QWP}} = 90$ deg, and $\theta_{\mathrm{QWP}} = -45$ deg. (e) Error in only the QWPs retardance with $\phi_{\mathrm{PG}} = 180$ deg, $\phi_{\mathrm{QWP}} = 45$ deg, and $\theta_{\mathrm{QWP}} = -45$ deg. (f) Error in both the PGs and QWPs retardance values with $\phi_{\mathrm{PG}} = 135$ deg, $\phi_{\mathrm{QWP}} = 45$ deg, and $\theta_{\mathrm{QWP}} = -45$ deg.

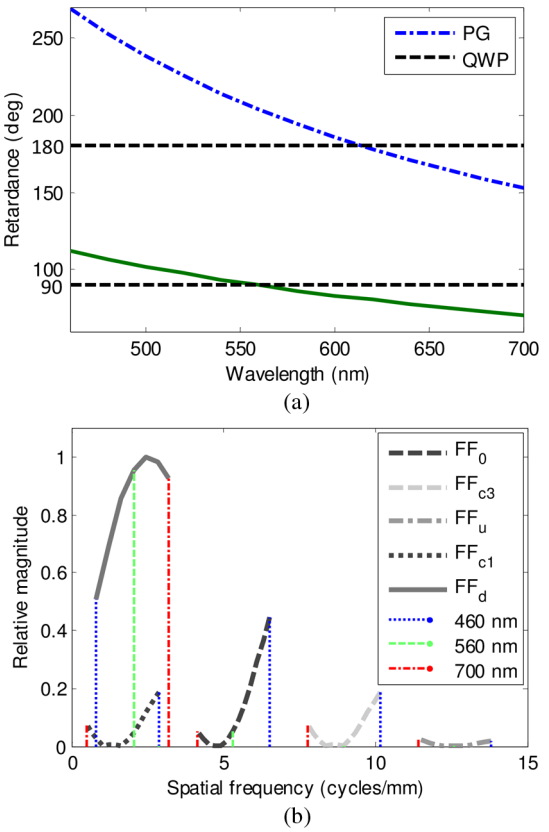

Fig. 4 (a) Simulated retardance spectra for a PG, with a layer thickness $d = 2.05$ μm, and a quartz QWP with a thickness of 15.27 μm. (b) Simulated frequency content of each component.

magnitude of the FF_d component corresponds to $\phi_{PG} = 180$ deg and that the multiplexing between FF_d and FF_{c1} is present due to simultaneous error in both ϕ_{PG} and ϕ_{QWP}.

3 Experimental Setup

A view of the system that was used to validate the theoretical model is depicted in Fig. 5. It consists of a diffuse source that illuminates a linear polarization generator (LPG). The LPG consisted of a linear polarizer with a transmission axis nominally oriented at $\theta_G = 135$ deg, where the angle is measured with respect to the x-axis. Light from the LPG was then incident onto a quartz WP that has an apex angle α of 6.2 deg. The two linear eigenpolarizations of the WP are oriented at 0 and 90 deg. An achromatic quarter wave plate (AQWP) follows the WP with a nominal orientation of $\theta_{QWP} = \pm 45$ deg such that the linear eigenpolarizations from the WP are converted into circular polarization states. A singlet, with a focal length $f = 100$ mm, was used to relay an image of the WP's wedge onto a PG with a lateral magnification $m_g = -1$. A variable iris was used to stop the lens down to reduce aberrations. It should be mentioned that this low power singlet was incorporated, as opposed to a multiple-element lens, to minimize polarization aberrations between the AQWP and the PG. The PG was patterned with polymerized liquid crystal with a spatial period of $\Lambda = 453$ μm and a peak first-order diffraction efficiency at $\lambda = 610$ nm. Light from the PG was then transmitted through a linear polarization analyzer, which consisted of a linear polarizer with a transmission axis nominally oriented at $\theta_A = 45$ deg. Finally, a 50 mm focal length c-mount objective lens imaged the interference pattern onto an 8-bit 1280×960 pixel element FPA.

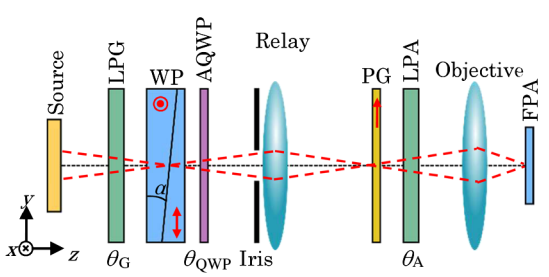

Fig. 5 Experimental setup of the PSHI. The PG's grating vector is indicated by the arrow, as are the WP's fast axis orientations.

The measured retardance spectrum of the AQWP is provided in Fig. 6(a). This measurement was taken by rotating the AQWP between crossed linear polarizers while measuring the transmitted spectrum using an Ocean Optics HR4000 spectrometer. The accuracy of this measurement is estimated at $\pm 0.25\%$. Meanwhile, the PG's retardance was calculated from the measured zero-order diffraction efficiency by fitting it to the theoretical closed-form expression

$$\mathrm{DE}_0(\lambda) = \cos^2(\phi_{PG}(\lambda)/2), \tag{45}$$

where $\phi_{PG}(\lambda)$ is used as the fitting parameter.[21] Using a least squares fitting procedure yielded the PG retardance depicted

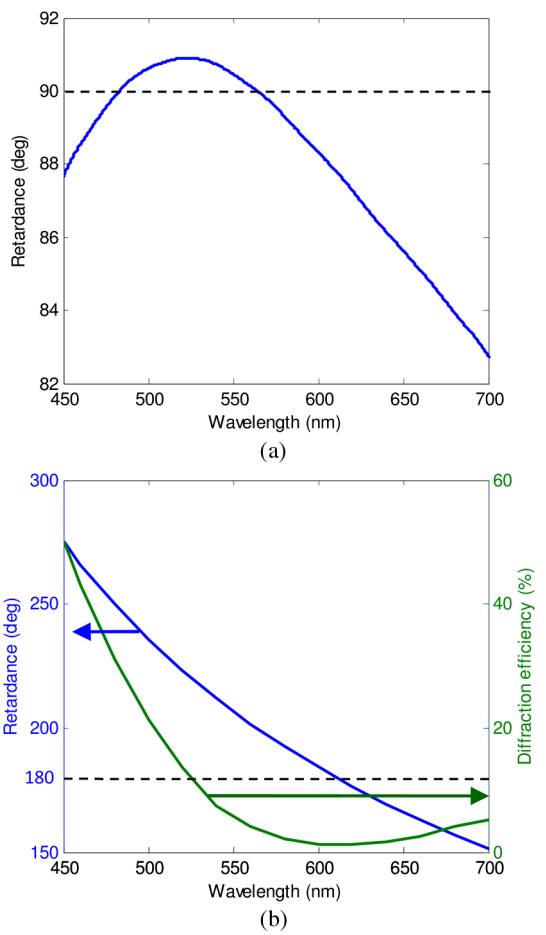

Fig. 6 Measured (a) achromatic QWP retardance spectrum and (b) PG zero-order diffraction efficiency and retardance spectra.

in Fig. 6(b). Here, ϕ_{PG} is a half wave at a wavelength of 610 nm, corresponding to the minimum zero-order diffraction efficiency.

4 Experimental Results

The experimental procedure for validating the model consisted of aligning the AQWP at $\theta_{QWP} = +45$ deg and $\theta_{QWP} = -45$ deg to up- and down-shift the prism's interference frequency, respectively. Light from a monochromator was used to illuminate the PSHI. The source's wavelength, λ_s, was varied from 460 to 700 nm in 20 nm increments and at each of these wavelengths a 2-D interference pattern was recorded. Since the interference components amplitude modulate the spectrum of the light source used in the monochromator, the spectrum's amplitude was removed by calibrating to a flat field at each wavelength.

In a procedure similar to Ref. 17, a flat field measurement was calculated at each monochromatic wavelength by acquiring two interferograms that are out-of-phase by 180 deg. The nominal interferogram, I_{G45}, was acquired with the LPG at $\theta_G = 45$ deg while the phase-shifted interferogram, I_{G135}, was acquired at an LPG orientation of $\theta_G = 135$ deg. These two interferograms can be expressed as

$$I_{G45}(x, y, \sigma_s) = TR|E(\sigma_s)|^2[16 + I_0 + I_{c1} + I_d + I_{c3} + I_u], \tag{46}$$

and

$$I_{G135}(x, y, \sigma_s) = TR|E(\sigma_s)|^2[16 - I_0 - I_{c1} - I_d - I_{c3} - I_u], \tag{47}$$

where T, R, I_0, I_{c1}, I_d, I_{c3}, and I_u are implicitly dependent on x, y, and σ_s for clarity and $\sigma_s = 1/\lambda_s$. Averaging Eqs. (46) and (47) yields a flat field containing only the spectral magnitude, optical transmission, and responsivity quantities such that

$$I_{Flat}(x, y, \sigma_s) = 16TR|E(\sigma_s)|^2. \tag{48}$$

A flat field measurement was calculated at both orientations of the QWP ($\theta_{QWP} = \pm 45$ deg) in order to account for polarization dependencies in the optical transmission. Interferograms of monochromatic spectra were then acquired by the PSHI such that

$$I_M(x, y, \sigma_s) = TRI_{out}(x, y, \sigma_s). \tag{49}$$

Normalization of Eq. (49) by (48) produces an interferogram without responsivity, optical transmission, or spectral dependencies.

After all monochromator interferograms were normalized to the flat field, an average across the FPA's x-dimension was taken in order to obtain a one-dimensional interferogram along y. Fourier spectra for each interferogram were then calculated per Eqs. (37)–(41). A summary of the experimental data is provided in Fig. 7 for both the (a) down-shifted (b) up-shifted cases. In each plot, the magnitude of the Fourier components for the experimental measurements (M) is plotted alongside the results from the theoretical model (T) for each channel. Due to the use of an achromatic QWP, minimal multiplexing is observed between FF_d and FF_{c1}. Hence, the most significant error is a result of zero-order light leakage

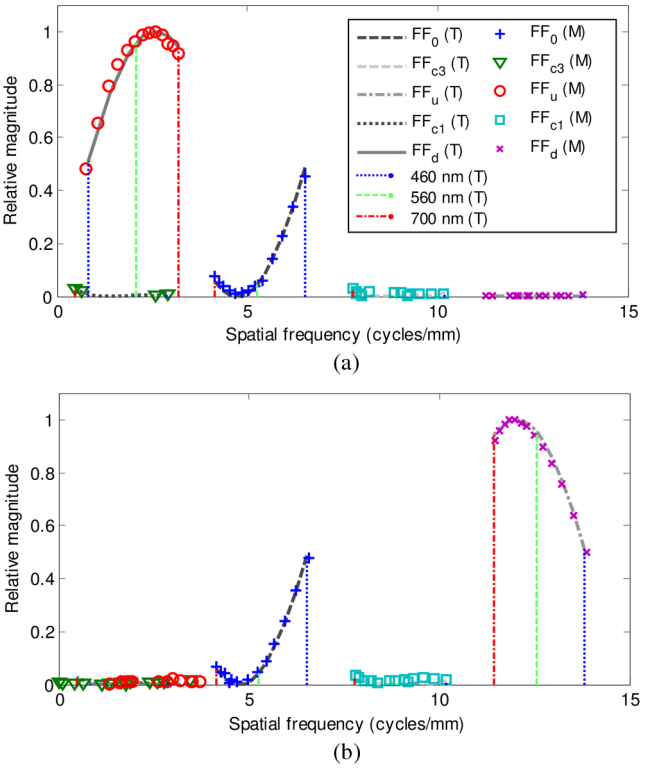

Fig. 7 Comparison between the theoretical model (*T*) and measurements (*M*) for QWP orientations of (a) $\theta_{QWP} = +45$ deg and (b) $\theta_{QWP} = -45$ deg. There is an excellent agreement between *T* and *M* for all wavelengths.

through the PG, which can be reduced by incorporating an achromatic PG.[22] It should be mentioned that this was not implemented in the current paper so that we could study the effects of zero-order light leakage.

The root-mean-square (RMS) error between the measured and theoretical Fourier components was calculated as

$$\text{RMS} = 100\sqrt{\frac{1}{N_s}\sum_{\sigma_s}^{N_s}(FF_{Theo}(\sigma_s) - FF_{Meas}(\sigma_s))^2}, \tag{50}$$

where N_s is the number of spectral measurements and FF_{Theo} and FF_{Meas} correspond to the theoretical and measured Fourier component magnitudes (e.g., FF_0, FF_d, FF_{c1}, etc.). The RMS error was calculated for each frequency component in both the up- and down-shifted datasets, the results of which are summarized in Table 1. Note that for FF_{c3} in the down-shifted data, only four data points were used where overlap did not occur with FF_d, per Fig. 7(a). The mean RMS error across all of the measured Fourier components is 1.02%, which is approximately equal to our experiment's estimated accuracy of 0.9% accounting for quantization error, alignment error in θ_{QWP}, and error in the measured values of ϕ_{PG} and ϕ_{QWP}.

5 Calibration Results

For most applications, the down-shifted spectra of Fig. 7(a) are of greatest utility. To account for linear mixing between the FF_d and FF_{c1} components in this configuration, a linear system model was used to spectrally calibrate the PSHI.[14,23] A matrix **H** was created such that

Table 1 Percent RMS error between theoretical and measured data for each Fourier component.

	FF_0	FF_{c3}	FF_u	FF_{c1}	FF_d
Up-shifted	1.07	1.32	1.19	0.84	1.03
Down-shifted	1.71	0.29	1.81	0.74	0.21

$$\mathbf{g} = \mathbf{H} \cdot \mathbf{f}, \tag{51}$$

where $\mathbf{H}$ is the system transfer matrix, $\mathbf{f}$ is the input spectrum, and $\mathbf{g}$ is the measured interferogram. The matrix $\mathbf{H}$ is configured with dimensions of OPD $\times \lambda$, such that each column contains a monochromatic interferogram.

Using the experimental setup, depicted previously in Fig. 5, the H-matrix's calibration performance was evaluated for calculating the output spectrum. This was conducted with the experimental setup depicted in Fig. 8, which depicts the inclusion of a 100-mm diameter integrating sphere (IS). An Ocean Optics HR4000 spectrometer, connected to the sphere via a 200-μm diameter fiber, was used to measure spectra for independent validation. The sphere was illuminated by either a white light tungsten halogen lamp or a monochromator. Optionally, the white light source could be filtered with removable gelatin filters. H-matrix characterization was accomplished using the monochromator. The monochromator was incremented from 420 to 720 nm in $N = 19$ increments with a uniform wave number spacing of $\Delta\sigma = 551\ \mathrm{cm}^{-1}$. This spectral resolution corresponds closely to the spectral resolution of the WP.

The measured H-matrix is depicted in Fig. 9. Notable is the presence of both the I_d and I_0 interference components that correspond to the high and low spatial frequency modulations versus y, respectively. As observed in the simulations, I_0 has increasing contrast for values of ϕ_{PG} away from 180 deg per Fig. 6(b). Calculating the pseudo-inverse of $\mathbf{H}$ enables the input spectrum to be calculated using

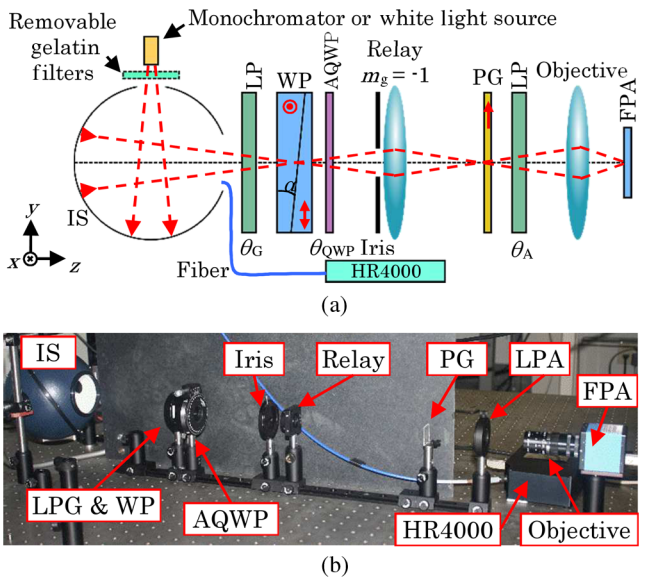

Fig. 8 (a) Schematic of the experimental setup for calibrating the PSHI and (b) photo of the system on the benchtop.

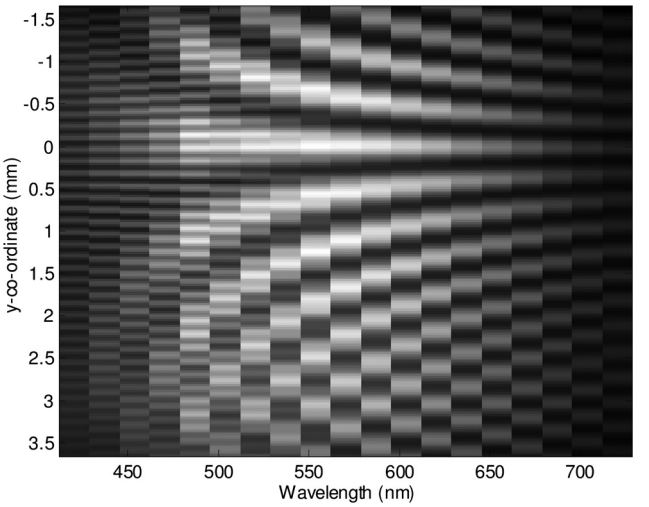

Fig. 9 Measured H-matrix.

$$\mathbf{f} = \mathbf{W} \cdot \mathbf{g}, \tag{52}$$

where $\mathbf{W}$ is the data reduction matrix, calculated from the pseudo-inverse functionality in MATLAB. Validation of the H-matrix calibration procedure was performed by illuminating the sphere with the white light tungsten halogen lamp. Spatially heterodyned interferograms were measured using the experimental setup, in addition to directly measured spectra that were acquired using the Ocean Optics HR4000 spectrometer. A white-light reference interferogram and spectrum were acquired first, followed by interferograms and spectra of four absorption gelatin filters (Roscolux brand, labeled F1 through F4) that were inserted between the lamp and integrating sphere. Spectra were then calculated, from the measured interferograms, by applying $\mathbf{W}$, and the transmission of each filter was calculated by dividing each of the filter's spectra by the white light reference spectrum. The transmission of each filter was also calculated from the HR4000 data for direct comparison. These results are depicted in Fig. 10 in which the ocean optics (OO) transmission spectra are plotted alongside the transmission spectra calculated from the PSHI.

The RMS error, averaged for all four transmission measurements, was calculated between the PSHI and OO data to be approximately 1.2% for these data.

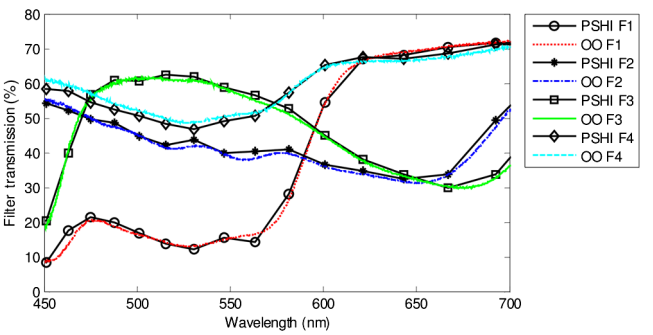

Fig. 10 Measured transmission data comparison from the PSHI and the OO spectrometer for filters F1 to F4.

6 Conclusion

In this paper, we successfully demonstrated a theoretical model and experimental calibration procedure for a PSHI. The interferometer was based on a WP that was heterodyned using a PG. As demonstrated by the model and subsequent experiments, nonideal frequency components are caused by the PG's zero-order light leakage and error in the QWP's retardance. Fortunately, low zero-order diffraction efficiencies (<3%) in the PGs are achievable using broadband multilayer achromatic PG designs.[22] Additionally, as demonstrated in the experiment, AQWPs can be leveraged to further reduce the undesirable frequency components. Finally, the H-matrix calibration procedure was implemented to calibrate the PSHI. This yielded an experimentally observed average RMS error of 1.2% when compared to an Ocean Optics spectrometer.

Acknowledgments

We gratefully acknowledge support from the National Science Foundation (NSF Grant No. ECCS-0955127).

References

1. P. Griffiths and J. A. D. Haseth, *Fourier Transform Infrared Spectrometry*, John Wiley & Sons (2007).
2. R. G. Sellar, G. D. Boreman, and L. E. Kirkland, "Comparison of signal collection abilities of different classes of imaging spectrometers," *Proc. SPIE* **4816**, 389–396 (2002).
3. D. Malacara, *Optical Shop Testing*, 3rd ed., Wiley-Interscience, Hoboken, NJ (2007).
4. J. Harlander, R. J. Reynolds, and F. L. Roesler, "Spatial heterodyne spectroscopy for the exploration of diffuse interstellar emission lines at far-ultraviolet wavelengths," *Astrophys. J.* **396**(2), 730–740 (1992).
5. G. G. Shepherd et al., "WINDII observations of the 558 nm emission in the lower thermosphere: the influence of dynamics on composition," *J. Atmos. Sol.-Terr. Phys.* **59**(6), 655–667 (1997).
6. G. Shepherd et al., "Windii, the wind imaging interferometer on the upper-atmosphere research satellite," *J. Geophys. Res. Atmos.* **98**(D6), 10725–10750 (1993).
7. J. M. Harlander et al., "Design and laboratory tests of a Doppler Asymmetric Spatial Heterodyne (DASH) interferometer for upper atmospheric wind and temperature observations," *Opt. Express* **18**(25), 26430–26440 (2010).
8. C. R. Englert, D. D. Babcock, and J. M. Harlander, "Doppler asymmetric spatial heterodyne spectroscopy (DASH): concept and experimental demonstration," *Appl. Opt.* **46**(29), 7297–7307 (2007).
9. D. A. Naylor et al., "Astronomical spectroscopy using an aliased step-and-integrate Fourier transform spectrometer," *Proc. SPIE* **5498**, 685–694 (2004).
10. D. Komisarek et al., "High-performance nonscanning Fourier-transform spectrometer that uses a Wollaston prism array," *Appl. Opt.* **43**(20), 3983–3988 (2004).
11. N. R. Gomer et al., "Raman spectroscopy using a spatial heterodyne spectrometer: proof of concept," *Appl. Spectrosc.* **65**(8), 849–857 (2011).
12. A. D. Meigs, "Common path interferometer for spectral image generation," U.S. Patent No. 6687007 B1 (2004).
13. M. W. Kudenov et al., "White light Sagnac interferometer for snapshot linear polarimetric imaging," *Opt. Express* **17**(25), 22520–22534 (2009).
14. A. V. Velasco et al., "Optical fiber interferometer array for scanless Fourier-transform spectroscopy," *Opt. Lett.* **38**(13), 2262–2264 (2013).
15. M. W. Kudenov et al., "Spatial heterodyne interferometry with polarization gratings," *Opt. Lett.* **37**(21), 4413–4415 (2012).
16. M. W. Kudenov et al., "Compact spatial heterodyne interferometer using polarization gratings," *Proc. SPIE* **8873**, 88730Q (2013).
17. M. W. Kudenov and E. L. Dereniak, "Compact real-time birefringent imaging spectrometer," *Opt. Express* **20**(16), 17973–17986 (2012).
18. M. J. Padgett and A. R. Harvey, "A static Fourier transform spectrometer based on Wollaston prisms," *Rev. Sci. Instrum.* **66**(4), 2807–2811 (1995).
19. R. C. Jones, "New calculus for the treatment of optical systems. VIII. Electromagnetic theory," *J. Opt. Soc. Am.* **46**(2), 126–131 (1956).
20. G. Cincotti, "Polarization gratings: design and applications," *IEEE J. Quantum Electron.* **39**(12), 1645–1652 (2003).
21. M. J. Escuti et al., "Simplified spectropolarimetry using reactive mesogen polarization gratings," *Proc. SPIE* **6302**, 630207 (2006).
22. C. Oh and M. J. Escuti, "Achromatic diffraction from polarization gratings with high efficiency," *Opt. Lett.* **33**(20), 2287–2289 (2008).
23. D. H. Goldstein, *Polarized Light*, CRC Press, Boca Raton, Florida (2011).

Michael W. Kudenov received his BS degree in electrical and computer engineering from the University of Alaska Fairbanks, Fairbanks, AK, in 2005 and his PhD degree in optical sciences from the University of Arizona, Tucson, AZ, in 2009. He is an assistant professor of ECE at North Carolina State University in Raleigh, NC. His lab researches compact high-speed hyperspectral, polarimetric, and interferometric sensors and sensing systems within multidisciplinary applications spanning remote sensing, defense, process monitoring, and biological imaging. He is a member of SPIE.

Matthew N. Miskiewicz received BS degrees in electrical engineering and computer engineering from North Carolina State University (NCSU) in 2006. He has since been a member of the Opto-Electronics and Lightwave Engineering Group, NCSU, working toward a PhD degree. His research focuses on FDTD methods, polarization holography, computer generated holograms, beam-combining, beam-shaping, beam-steering, and novel direct-write systems.

Michael J. Escuti received his PhD degree in electrical engineering from Brown University, Providence, RI, in 2002. Currently, he is an associate professor of electrical and computer engineering at North Carolina State University (NCSU) at Raleigh, where he pursues interdisciplinary research in photonics, opto-electronics, flat-panel displays, diffractive optics, remote sensing, and beyond. He is a named inventor on 17 issued and 12 pending patents, has published more than 93 refereed journal and conference publications, presented 24 invited talks, and has coauthored one book chapter. He is a member of SPIE.

James F. Coward is cofounder and president/CEO of SA Photonics, where he leads development of photonic sensing and communication systems. He has been the system architect/principal engineer on hardware fielded in many market segments, including mission critical sensor hardware flying on over 20 satellites, critical cockpit display hardware on every F18 E/F in the world, mission critical hardware in the terrestrial telecom, and semiconductor inspection industries.